Current Biology, Volume *35*

Supplemental Information

Synchronization in epithelial tissue morphogenesis

Prachi Richa, Matthias Häring, Qiyan Wang, Ankit Roy Choudhury, Martin C. Göpfert, Fred Wolf, Jörg Großhans, and Deqing Kong

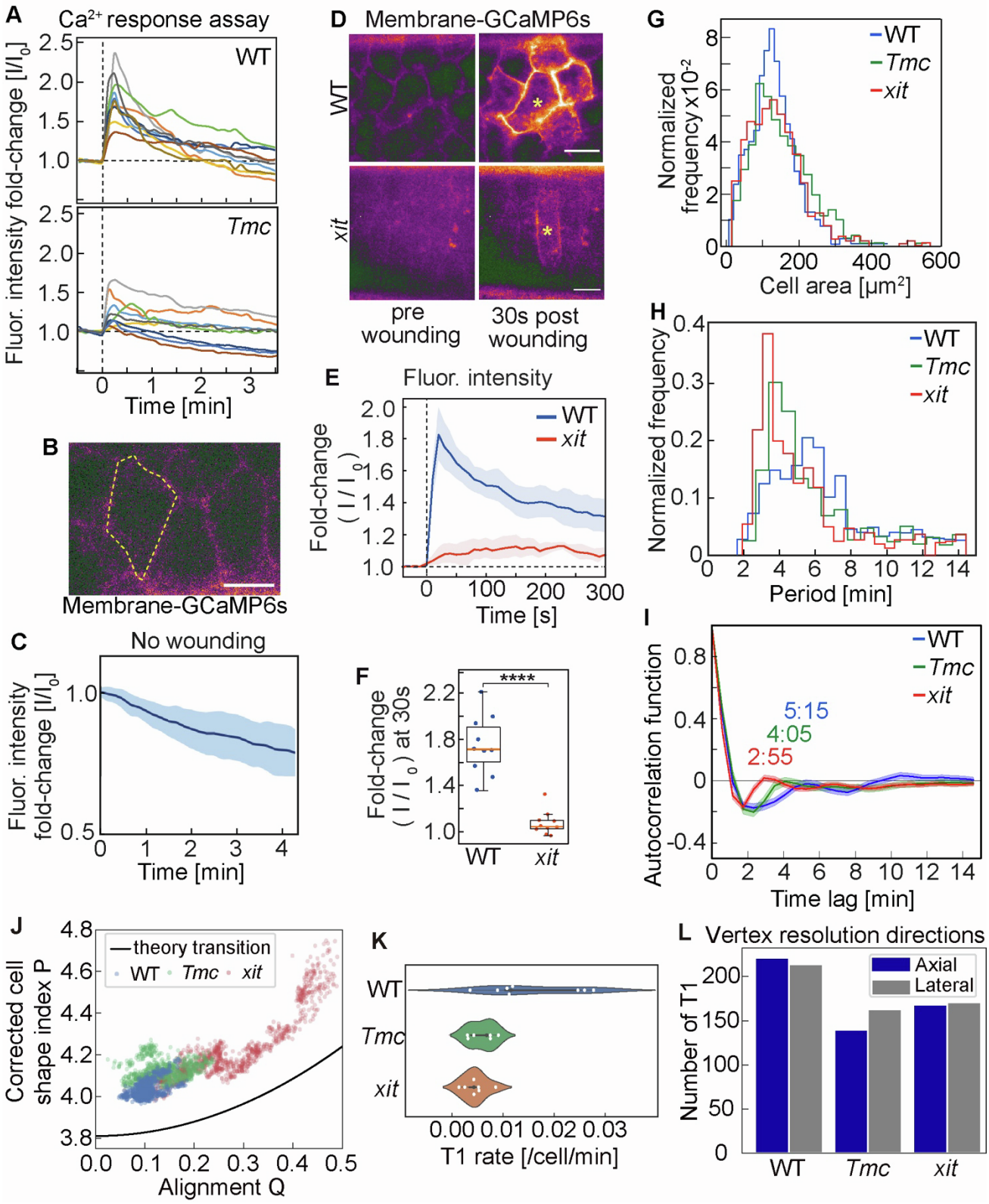

Figure S1. Ca^{2+} response assay in AS cells, tissue fluidity and the parameters of cellular morphology and dynamics during the elliptical stage, related to Figures 1 and 2.

(A) Individual traces of normalized GCaMP6s fluorescence at junctions of neighbors in wounding experiments. Laser induced wounding at T=0.

(B) Image from a living embryo expressing the membrane Ca^{2+} sensor (myr-GCaMP6s). The dashed yellow line marks the cell outline. Scale bar 10 μm.
(C) Fluorescence trace of Ca^{2+} sensor without wounding indicating the degree of bleaching of GCaMP6s.
(D) Time-lapse imaging of neighbor cell dependent Ca^{2+} response. Images 10 s before and 30 s after wound induction in the marked target cell in embryos of wild type and *xit* mutant.
(E) Time course of Ca^{2+} sensor fluorescence (mean (solid line) and 95% bootstrap confidence interval (band)). Wounding at t=0. N=10 embryos per genotype.
(F) Normalized fluorescence of Ca^{2+} sensor 30 s after wounding. Statistical significance by *student t-test*. P values = 3.6e-07.
(G) Distribution of apical cross-section area.
(H) Distributions of cell oscillation periods determined via wavelet transform.
(I) Autocorrelation functions of the area trajectories. Average with confidence band. Numbers indicate the major periods of the oscillations.
(J) Geometrical indicators of tissue fluidity for the three mutants. The black line indicates the theoretical transition between solid-like and fluid-like tissue. Each dot represents one frame from the time-lapse recordings of the AS. Statistical significance of distribution difference according to a 2d Kolmogorov-Smirnov test: WT-*Tmc* p=8e-117, WT-*xit* p=5e-186, *Tmc*-*xit* p=3e-99.
(K) T1 transition rate for every embryo (dots). Statistical significance of distribution difference according to a Kolmogorov-Smirnov test: WT-*Tmc* p=0.012, WT-*xit* p=0.002, *Tmc*-*xit* p=0.58.
(L) Direction of T1 vertex resolution. Statistical significance according to chi-squared test against uniform H0: WT p=0.73, *Tmc* p=0.19, *xit* p=0.87.

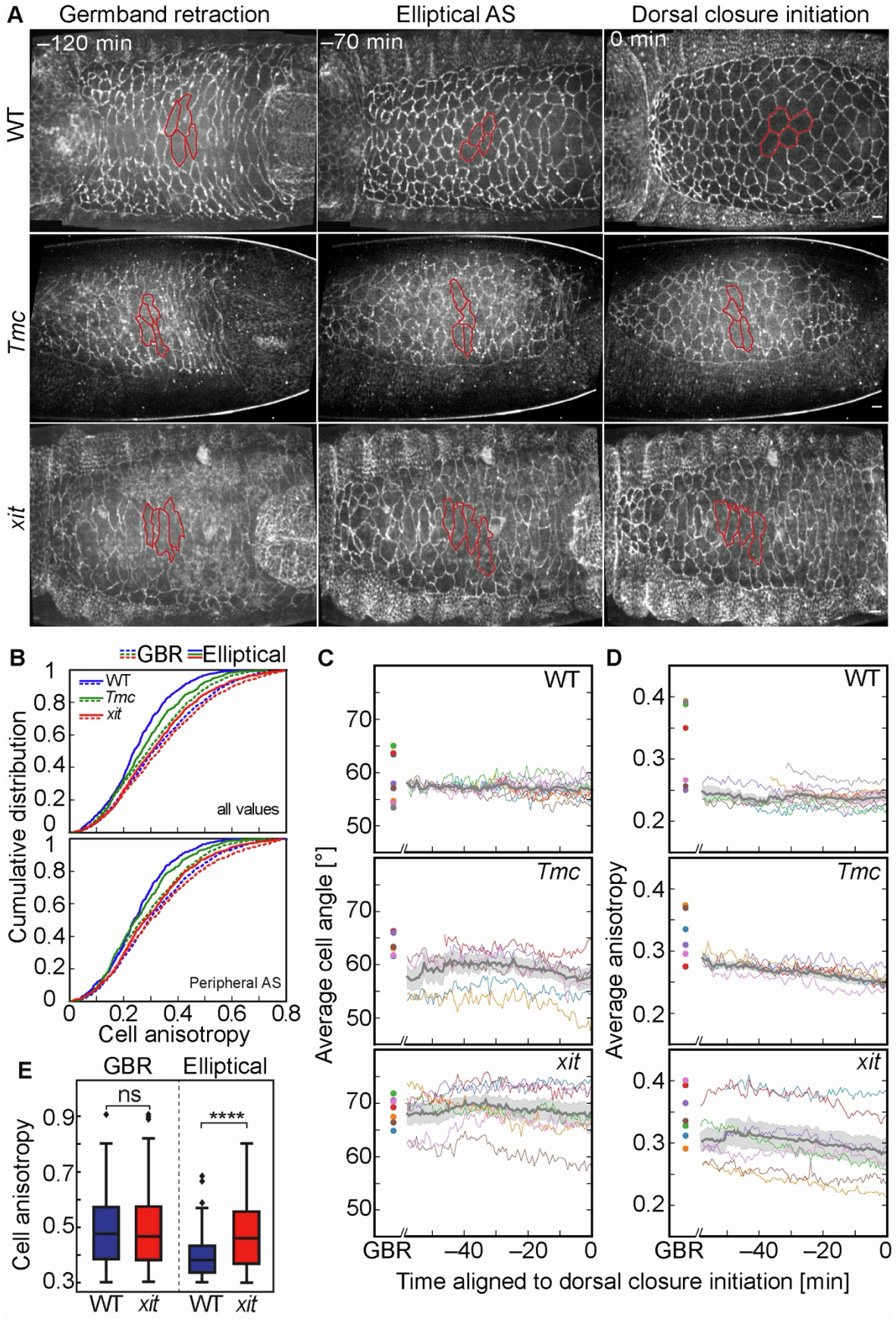
A
Germband retraction
Elliptical AS
Dorsal closure initiation
–120 min
–70 min
0 min
WT
Tmc
xit
B
GBR
Elliptical
WT
Tmc
xit
all values
Peripheral AS
Cumulative distribution
Cell anisotropy
C
Average cell angle [°]
D
Average anisotropy
GBR
–40
–20
0
Time aligned to dorsal closure initiation [min]
E
GBR
Elliptical
ns
****
Cell anisotropy
WT
xit
WT
xit

Figure S2. Cell shape changes during germband retraction and elliptical stage, related to Figure 2
(A) Images from time-lapse recordings of wild-type, *Tmc*, and *xit* mutants. Dorsal view, axial projections. Junction labeled by E-cadherin-GFP. A few cells are outlined in red, indicating the cell shape changes.
(B) Cumulative distributions of cell anisotropy separately for all values and peripheral cells during indicated stages.
(C) Time course for the average orientation of AS cells for each embryo. Mean and standard deviation averaged over embryos are indicated by grey line and band. Angle is normalized between the axial axis and lateral axis. Dots indicate average values during germband retraction.
(D) Time course of the average shape anisotropy for each embryo. The grey line and band indicate the mean and standard deviation averaged over embryos. Dots indicate average values during germband retraction.
(E) Distribution of cell shapes with an anisotropy larger than 0.3 indicated by boxplots in wild-type and *xit* embryos. Statistical significance: p-value = 8.3e-08; two-sided *Mann–Whitney test*. WT, n=8 embryos, 436 cells; *xit*, n=7 embryos, 238 cells.

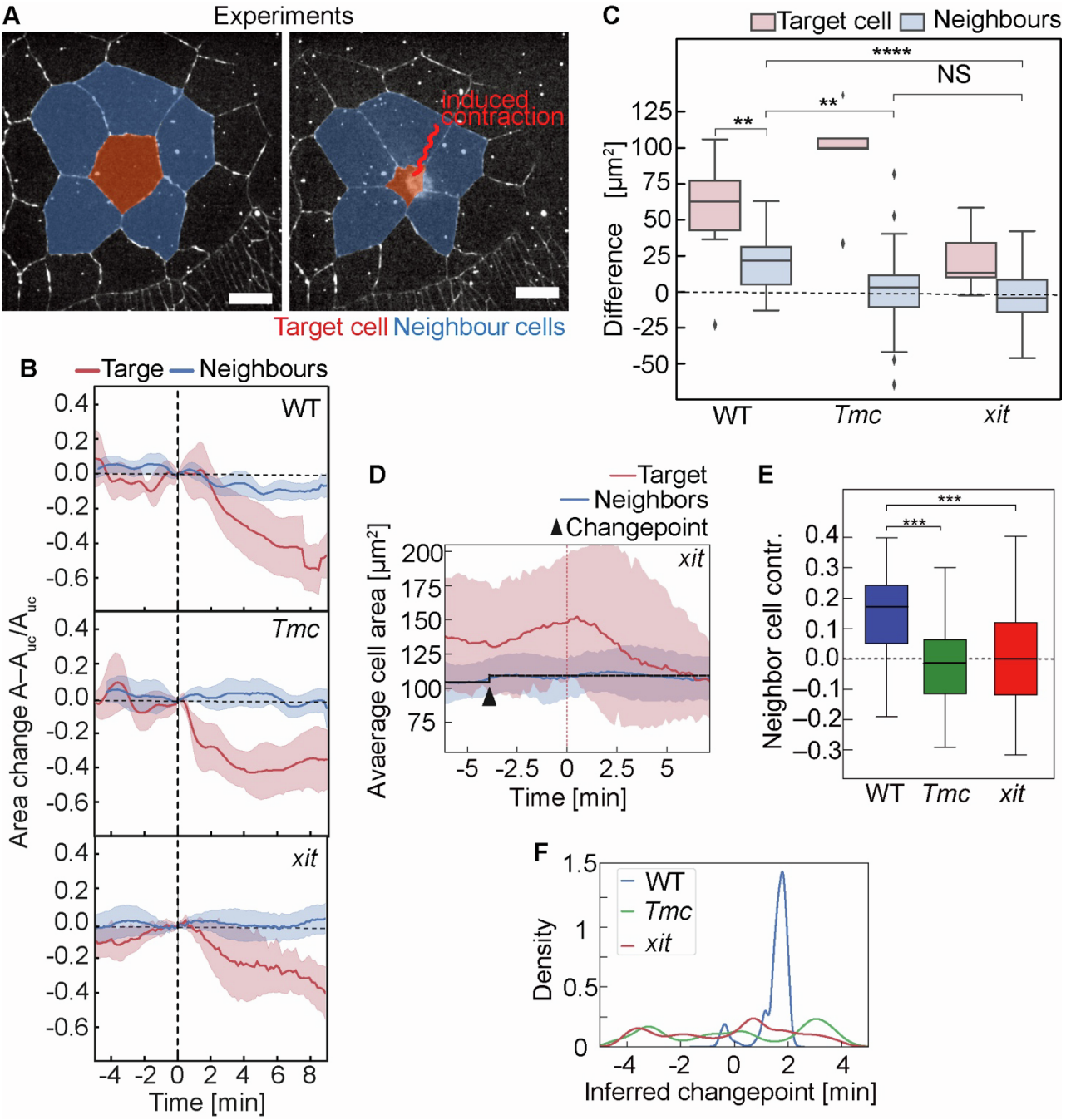

Figure S3. Response of neighbors to triggered contraction of a target cell, related to Figure 3.

(A) Experimental scheme for *in vivo* triggered contraction of the target cell (red) by Ca^{2+} uncaging. Area trajectories for the next neighbors (blue) were recorded.

(B) The trajectories of area change in target cells (red) and next neighbors (blue) after triggered contraction in the target cell by Ca^{2+} uncaging at 0 min. Solid lines indicate average bands with a 95% bootstrap confidence interval.

(C) Area difference of target cell and neighbors between the time of uncaging and 6 min after that.

(D) Ensemble averaged cell areas across in *xit* mutant. Bands represent 95% bootstrap confidence interval. Black triangles denote the detected change points for the ensemble mean of the neighbor cell areas (blue). Gray lines indicate the average area before and after the changepoint. Time relative to opto-chemical trigger event at t=0.

(E) Measured *in vivo* area contractions in neighbors in wild type, *Tmc* and *xit* mutants. P-values calculated via the *Mann-Whitney-Wilcoxon test*. ***, 1.0e-04 < p <= 1.0e-03. WT-*Tmc* p= 1.3e-04 (same data in Figure 3D), WT-*xit* p= 4.9e-04. N_{WT}=48, N_{Tmc}=28, N_{xit}=34.
(F) Distribution of changepoint estimates (kernel density estimate from 10000 bootstrapped changepoint inferences).

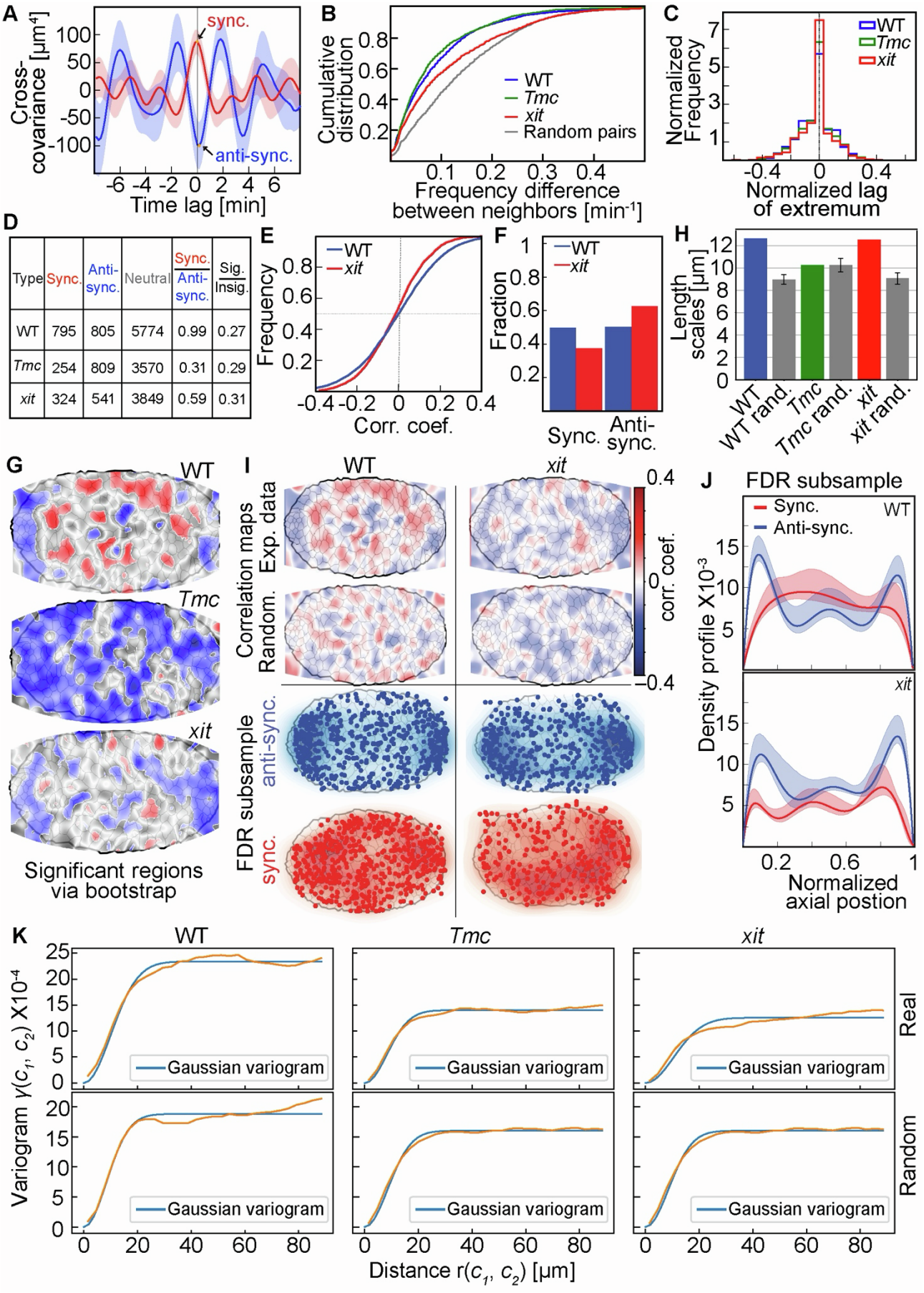
A
Cross-covariance [μm⁴]
sync.
anti-sync.
Time lag [min]
B
Cumulative distribution
WT
Tmc
xit
Random pairs
Frequency difference between neighbors [min⁻¹]
C
Normalized Frequency
WT
Tmc
xit
Normalized lag of extremum
D
Type | Sync. | Anti-sync. | Neutral | Sync./Anti-sync. | Sig./Insig.
WT | 795 | 805 | 5774 | 0.99 | 0.27
Tmc | 254 | 809 | 3570 | 0.31 | 0.29
xit | 324 | 541 | 3849 | 0.59 | 0.31
E
Frequency
Corr. coef.
F
Fraction
Sync.
Anti-sync.
H
Length scales [μm]
WT
WT rand.
Tmc
Tmc rand.
xit
xit rand.
G
Significant regions via bootstrap
I
Correlation maps
Exp. data
Random.
FDR subsample
anti-sync.
sync.
corr. coef.
J
FDR subsample
Density profile X10⁻³
Normalized axial postion
K
Variogram γ(c1, c2) X10⁻⁴
Gaussian variogram
Real
Random
Distance r(c1, c2) [μm]

Figure S4. Synchronization and subsampling analysis, related to Figure 5

(A) Exemplary cross-covariance of a synchronized cell pair (red) and an anti-synchronized cell pair (blue). Time lag for both coupling types marked with an arrow.

(B) The difference in oscillation frequency in cell pairs is shown by the cumulative distribution.

(C) Time lag of the extremum in the cross-correlation functions between neighboring cells plotted as a histogram.

(D) Numbers of cell pairs for correlation analysis from the complete data set. Neutral cases have a local false discovery rate>0.1.

(E) Cumulative distribution of correlation coefficients of all cell pairs computed over the complete elliptical stage. Statistical significance of distribution difference according to a Kolmogorov-Smirnov test: WT-*xit* p=2e-27.

(F) Proportion of sync and anti-sync cell pairs among cell pairs with statistically significant coupling. Wild type, 8 embryos 7370 pairs with 795 sync, 801 anti-sync significant coupling; *xit,* 7 embryos with 4714 pairs with 324 sync, 541 anti-sync significant coupling. Statistical significance of frequency difference according to chi-squared test: WT-*xit* p=4e-16.

(G) Significant regions of the correlation maps determined via bootstrapping over the embryos.

(H) Length scales of correlation maps determined by variogram analysis and fit to Gaussian random field. The comparison of length scales from the original correlation map with its randomized version shows that there is a significant spatial order for wild type and *xit* maps but not for the *Tmc* map.

(I) Maps of correlation coefficients kernel-averaged from wild type (same data in Figure 5F) and *xit* mutant. Below each map, randomized correlation maps are displayed. Hereby, measured correlation coefficients were reassigned to randomly chosen junctions. FDR subsample maps: Positions of cell junctions for (anti-)synchronized pairs subsampled via controlling the local false discovery rate.

(J) Spatial density profile of FDR subsampled junctions from wild type (same data in Figure 5G) and *xit* mutant.. Confidence bands were computed by bootstrapping over embryos.

(K) Fits of theoretical Gaussian variogram (bestfit in blue) to the measured variogram (orange).

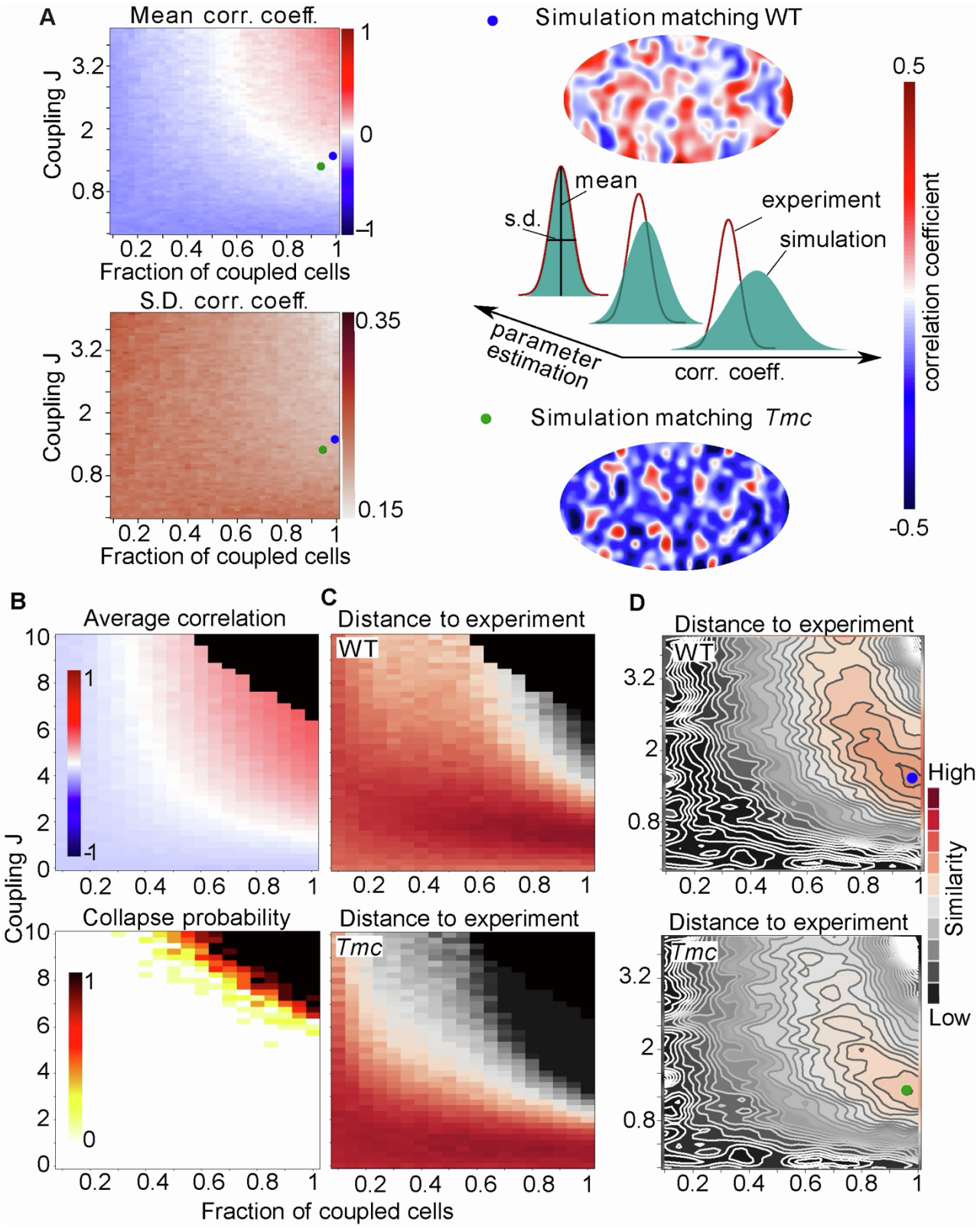

Figure S5. Quantification of similarity between simulations and experimental data, related to Figures 4 and 5.

(A) Mean and standard deviation of correlation coefficients for simulations as a function of coupling strength and fraction of coupled cells. For a fraction of one, every cell pair in the tissue is equipped with mechano-chemical coupling. Simulations were repeated 20 times for each parameter set and the mean and standard

deviation of the distribution of correlation coefficients evaluated. For weak or absent coupling, cells are on average moderately anti-correlated. Parameters were optimized for matching the experimental distribution of correlation coefficients. Samples of correlation maps predicted by the model for best-matching parameters are shown. This shows that, in principle, the fraction of coupled cells (e.g. heterogeneous distribution of *Tmc)* can alter the correlation distribution. However, inference suggests that a homogeneous distribution of the mechano-chemical coupling mechanism has the highest likelihood.
(B) Same plots as in (A), here with extended parameter range for coupling strength *J*. Blacked regions are collapsed simulations in more than 30% of simulations. In addition, the collapse probability is shown.
(C) The distance between the model and experiment was quantified by the Jensen divergence between the distribution of correlation coefficients.
(D) Same as (C) but showing relevant parameter region and additional contour lines for clarity. Blue and green dots mark maximum a posteriori estimates of model parameters obtained by nested sampling.

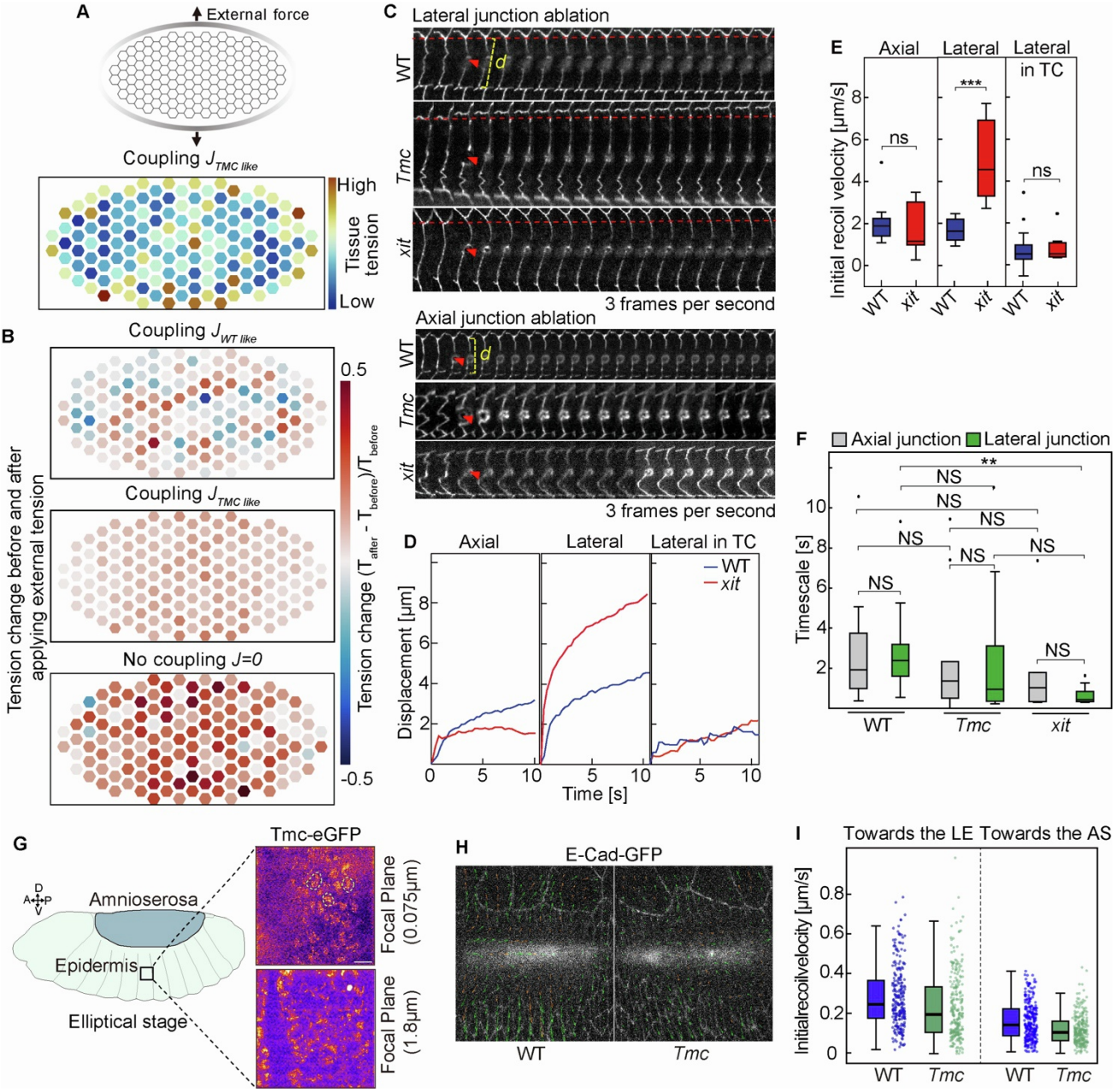

Figure S6. Simulation and experimental detection of tissue-scale tension distribution in response to epidermal pulling force and tissue-scale tension in lateral epidermis, related to Figure 6

(A) External tension was applied perpendicular to the AS in order to mimic pulling by the lateral epidermis as described in Figure 6A. Below: similar scheme like in Figure 6A but for *Tmc* like parameters, showing tension in individual cells.

(B) Tension changes in cells in AS simulation. First, the simulation ran long enough to equilibrate without external force, then external force was applied and simulation ran again until equilibration. Colors denote the change in tension before and after applying the external force.

(C) Kymographs of representative experiments with junctions in lateral (up) or axial (bottom) orientations. Arrow head in red points to position of laser application. Displacement d is the change in the distance between the adjacent 3x vertices indicated by dashed line in yellow.

(D) Representative displacement curves following junction cuts (wild type data same in Figure 6D).

(E) Initial recoil velocities (wild type data same in Figure 6E). One micro dissection experiment was performed per single embryo (n=10 embryos for each genotype and condition. Statistical significance by *Student's t-test*. ns, p>0.05, **p<0.01, ***p<0.0001).
(F) Time scales calculated by fitting of a viscoelastic element to the displacement traces. Statistical significance by *Student's t-test,* ns, p>0.05, **p<0.01.
(G) Live imaging in the lateral epidermis, from an embryo expressing Tmc-eGFP using a GFP tag introduced at the C-terminus of *Tmc* at the endogenous gene locus. The images were captured from apical or junctional planes; the dashed while line marks the cell outline.
(H) Images from the time-lapse recording after the laser ablation. E-CadGFP outlines cells. The green arrow lines indicate the velocity vectors performed by particle image velocimetry (PIV) analysis. The length of vectors represents the magnitude of the recoil velocity.
(I) Quantification of the recoil velocity from vertically (lateral orientation). Boxplot shows the initial recoil velocities after tissue ablation. Boxes, second and third quartiles; whiskers, 95% confidence interval; horizontal line, mean. Dots are the data outside of confidence interval. Three independent experiments from 3 embryos in each genotype, N=252 vectors Toward the LE and AS respectively. Statistical significance by *Student's t-test*, WT-*Tmc* (Toward the LE) p= 1.4e-03; WT-*Tmc* (Toward the AS) p=6.9e-08.

Data S1. Modeling of intercellular coordination in the amnioserosa, related to Figures 4 and S5

In order to investigate intercellular synchronization computationally, we used a cell-based model, where single cell units are operating on a triangular lattice. They are interacting via mechanical interactions and are additionally coupled via mechanosensitive Ca^{2+} activation that in turn activates myosin.

Conceptual model

The dynamics of a single cell unit is realized as a system of three coupled differential equations for the cell area *A*, the myosin concentration *m* and amount of Ca^{2+}-ions *c*. Colored terms denote extensions of Dierkes' model [S1].

$$\mu \frac{\mathrm{d}A}{\mathrm{d}t} = T_e - T(m) - K(A) + \xi(t) \tag{1}$$

$$\frac{\mathrm{d}m}{\mathrm{d}t} = -\frac{1}{\tau_m}(m - m_0) - \frac{m}{A}\frac{\mathrm{d}A}{\mathrm{d}t} + \alpha \frac{c}{A} \tag{2}$$

$$\frac{\mathrm{d}c}{\mathrm{d}t} = J\Theta\left(\dot{A}^{(n)}\right)\Theta\left(\dot{A}^{(n)} + \dot{A}\right) - c/\tau_c \tag{3}$$

With the abbreviations:

$$T(m) = T(m_0) + t_1(m - m_0)$$
$$K(A) = K(A_0) + k_1(A - A_0) + k_3(A - A_0)^3$$
$$T_e = T(m_0) + K(A_0)$$
$$\Theta(x) = \frac{1}{1 + \exp(\beta x)}, \beta \gg 1$$

whereas $T(m)$ is the myosin induced contractile force, T_e the equilibrium tension and $K(A)$ the intrinsic spring force. For a full discussion of these terms see [S1]. The noise $\xi(t)$ is a Gaussian random force.

$$\langle \xi(t) \rangle = 0$$
$$\langle \xi(t)\xi(t') \rangle = 2D\delta(t - t')$$

$\Theta(x)$ is the activation function for the mechano-sensitive ion channels. In this study β is chosen such that the activation effectively is heaviside-like, but in principle smoother activation is possible. The argument $\dot{A}^{(n)}$ denotes the change in area in a neighbor cell *n*. In the simulation we use the difference in tension at the interface between the two cells, however for readability reasons we simply write $\dot{A}^{(n)}$ here. The parameter *J* controls the strength of the novel calcium coupling mechanism.

Two-cell model

A simple first test of the model is its realization as a linear chain, but only with two elements. In this simplified system it is easy to get a feeling for the novel calcium coupling extension.
The basic equations for the linear chain, as depicted in Fig. 1, read

$$\lambda \frac{\mathrm{d}x_n}{\mathrm{d}t} = f_n - f_{n-1} \tag{4}$$

$$f_n = T(m_n) + K(A_n) + \mu \frac{\mathrm{d}A_n}{\mathrm{d}t} \tag{5}$$

These equations are an application of Kelvin-Voigt viscoelastic dynamics to the border dynamics [S2]. Here, x_n denotes the position of the nth cell border in the linear chain. The 1D 'area' of a cell thus is $A_n = x_{n+1} - x_n$. Myosin and calcium dynamics do not change compared to (2). We reduce this chain of n cells to 2 cells.

$$\lambda \frac{\mathrm{d}x_0}{\mathrm{d}t} = T(m_1) + K(A_1) - k_{ext}(x_0 - x_0^0) + \mu \frac{\mathrm{d}(x_1 - 2x_0)}{\mathrm{d}t} \tag{6}$$

$$\lambda \frac{\mathrm{d}x_1}{\mathrm{d}t} = T(m_2) + K(A_2) - T(m_1) - K(A_1) + \mu \frac{\mathrm{d}(x_2 - 2x_1 + x_0)}{\mathrm{d}t} \tag{7}$$

$$\lambda \frac{\mathrm{d}x_2}{\mathrm{d}t} = -T(m_2) - K(A_1) - k_{ext}(x_2 - x_2^0) + \mu \frac{\mathrm{d}(-2x_2 + x_1)}{\mathrm{d}t} \tag{8}$$

We see that we can write this system in terms of a mass-matrix on the left hand side and the sum of forces on the right hand side since *x* appears only linearly on both sides

$$M\vec{\dot{x}} = \vec{F}(\vec{x}) \tag{9}$$

where

$$M = \begin{pmatrix} \lambda + 2\mu & -\mu & 0 \\ -\mu & \lambda + 2\mu & -\mu \\ 0 & -\mu & \lambda + 2\mu \end{pmatrix} \tag{10}$$

and

$$\vec{F}(\vec{x}) = \begin{pmatrix} T(m_1) + K(A_1) - k_{ext}(x_0 - x_0^0) \\ T(m_2) + K(A_2) - T(m_1) - K(A_1) \\ -T(m_2) - K(A_1) - k_{ext}(x_2 - x_2^0) \end{pmatrix} \tag{11}$$

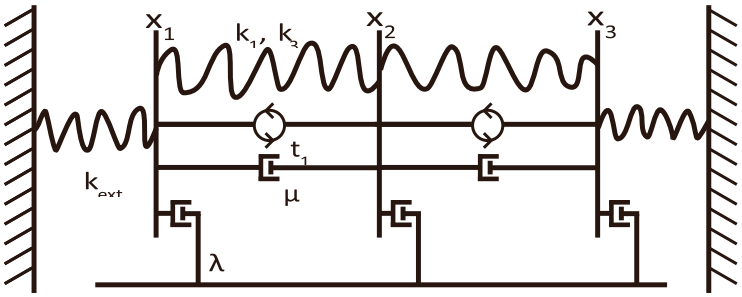

Figure 1: Linear chain model for two cells.

This system is used to calculate the phase diagram including synchronization in the main text.

Model on triangular lattice

The amnioserosa epithelium is modeled as single cell units which follow the dynamics described in the previous sections and are arranged on a triangular lattice. This model is comprised of one dimensional limit-cycle oscillators on a grid, with connections determined by an interaction matrix. The system of equations for a single cell unit *i* read

$$\left(\frac{\lambda}{N} + \mu\right)\frac{\mathrm{d}A^{(i)}}{\mathrm{d}t} = F^{(\text{internal})} + F^{(\text{external})} + F^{(\text{noise})} \tag{12}$$

$$= -T\left(m^{(i)}\right) - K\left(A^{(i)}\right)$$

$$= -\frac{1}{N}\sum_{n=1}^{N}\left[\mu\frac{\mathrm{d}A^{(n)}}{\mathrm{d}t} + T\left(m^{(n)}\right) + K\left(A^{(n)}\right) - \xi^{(n)}\right] + \xi^{(i)} \tag{13}$$

$$\frac{\mathrm{d}m^{(i)}}{\mathrm{d}t} = -\frac{1}{\tau_m}\left(m^{(i)} - m_0\right) - \frac{m^{(i)}}{A^{(i)}}\frac{\mathrm{d}A^{(i)}}{\mathrm{d}t} + \alpha\frac{c^{(i)}}{A^{(i)}} \tag{14}$$

$$\frac{\mathrm{d}c^{(i)}}{\mathrm{d}t} = \sum_{n=1}^{N}\left[J^{(n)}\Theta\left(\dot{A}^{(n)}\right)\Theta\left(\dot{A}^{(n)} + \dot{A}^{(i)}\right)\right] - \frac{1}{\tau_c}c^{(i)} \tag{15}$$

The index *i* denotes cells on the lattice sites, *n* runs over the N neighbors (N=6 for hexagonal configuration). Myosin and calcium dynamics remain mostly unchanged except for summing all contributions from neighboring cells to obtain the total calcium influx.
External mechanical forces $F^{(external)}$ are comprised of the total internal force acting inside neighboring cells. We simplify by assuming that the force is distributed isotropically among all 6 neighboring cells and thus the external force component acting on cell *i* from cell *j* is $F_{ij}^{(internal)}/6$ in case of a triangular lattice.

The substrate friction λ causes dissipation of energy as cells move across a substrate. Biologically, this is motivated by the amnioserosa lying above the yolk of the developing embryo.

Boundary and external tension

Since the amnioserosa roughly features an elliptical shape we also employ such a geometry. Fully unconstrained cell units are arranged on a triangular lattice with periodic boundary conditions. We chose an ellipse with ratio of the half axes a/b = 1/2 and determine *a* and *b* such that we have around 150 cells in the tissue. Cells outside this ellipse are called border cells and follow different dynamics. They are simple relaxators consisting only of contractile elements with spring constants k_{ext}. There is mechanical coupling to the cells from the tissue but no myosin or calcium compartments. By tuning k_{ext} we can set constraints on the total tissue area.
External tension is applied as constant force applied to all border cells. We assume that the epidermis exerts a pulling force perpendicular to the AP axis of the tissue. Therefore, the effective external force acting on a border cell is highest for the middle cells, where the tangent of the AS border is aligned with the AP axis. The local external force declines towards the canthi, which is realized by a cosine weight depending on the *x* position along the AP axis, where *x* = 0 is exactly in the middle of the tissue.

Simulations

The model is implemented and optimized in Julia [S3]. A single simulation of the 2D model with 150 cells (450 coupled DEs + noise) completes in 2-3 minutes on a single core of a 8 year old laptop with an Intel i5 2.50 GHz processor. For parameter searches, nested sampling and repeated simulations the code can be parallelized. Integration of the system of stochastic differential equations is done via the Julia package ”DifferentialEquations.jl” [S4]. Because the model becomes unstable for certain parameter combinations, we employ an adaptive solver that takes smaller timesteps to maintain convergence if needed [S5]. We tested and compared different solvers, for instance an implicit Euler scheme, and we picked a solver that empirically showed the best performance and stability.

Parameter Inference

We compare the simulations of the model with experimental data by utilizing the distribution of correlation coefficients between neighboring cells as metric for the overall degree of synchronization. Since we compare

distributions, a cross entropy measure is chosen to evaluate the model likelihood. In particular we use the Jensen-Shannon divergence, a symmetric version of the Kullback-Leibler distance, between the *in vivo* and *in silico* distributions.

The Kullback-Leibler distance is defined as

$$D_{KL}\left(p^{(\text{simulation})} \| q^{(\text{experiment})}\right) = \sum_i p(x_i) \log \frac{p(x_i)}{q(x_i)} \tag{16}$$

The Kullback-Leibler divergence is minimized by the maximum likelihood estimate which can be swiftly calculated

$$\hat{\theta} = \arg\max_{\theta} \prod_{i=1}^{N} p(x_i \mid \theta) \tag{17}$$

$$= \arg\max_{\theta} \sum_{i=1}^{N} \log p(x_i \mid \theta) \tag{18}$$

$$= \arg\max_{\theta} \frac{1}{N} \sum_{i=1}^{N} \log p(x_i \mid \theta) - \frac{1}{N} \sum_{i=1}^{N} \log p(x_i \mid \theta_0) \tag{19}$$

$$= \arg\max_{\theta} \frac{1}{N} \sum_{i=1}^{N} \log \frac{p(x_i \mid \theta)}{p(x_i \mid \theta_0)} \tag{20}$$

$$\xrightarrow[N\to\infty]{} \arg\min_{\theta} \int \log \frac{p(x \mid \theta_0)}{p(x \mid \theta)} p(x \mid \theta_0)\, \mathrm{d}x \tag{21}$$

This is intuitively clear because minimizing the distance between the 'real' distribution with correct parameters θ_0 and the model distribution with parameters θ ultimately leads to the closest representation of the data that is possible for a given model.

Then we obtain the Jensen divergence in the following way

$$D_{JS}(p\|q) = \frac{1}{2} D_{KL}(p\|M) + \frac{1}{2} D_{KL}(q\|M) \tag{22}$$

with

$$M = \frac{1}{2}\left(p^{(\text{simulation})} + q^{(\text{experiment})}\right) \tag{23}$$

The Jensen divergence is a similar distance metric with the advantage to yield symmetric distances while the Kullback-Leibler divergence is dependent on the order of model and simulation distribution.

Parameter optimization is performed utilizing nested sampling [S6]. The parameter space is first uniformly sampled and then subsequently constrained via multi-ellipsoidal fits to the existing live points. In Julia, we use the package "NestedSamplers.jl" [S7], which is similar to MultiNest [S8]. Simulations were performed using the following parameters: $\mathrm{k}_1 = 1$, $\mathrm{k}_3 = 15$, $\mathrm{t}_1 = 2.1$, $\mu = 0.5$, $\mathrm{k}_{\mathrm{ext}} = 0.001$, $\lambda = 0.9$, $\mathrm{D} = 0.001$, $\mathrm{m}_0 = 1$, $\mathrm{A}_0 = 1$, $\tau = 1$, $\tau_{\mathrm{m}} = 1$.

Supplemental References

S1. Dierkes, K., Sumi, A., Solon, J., and Salbreux, G. (2014). Spontaneous Oscillations of Elastic Contractile Materials with Turnover. Physical Review Letters *113*, 148102. 10.1103/PhysRevLett.113.148102.

S2. Meyers, M.A., and Chawla, K.K. (2008). Mechanical behavior of materials (Cambridge university press).
S3. Bezanson, J., Edelman, A., Karpinski, S., and Shah, V.B. (2017). Julia: A Fresh Approach to Numerical Computing. SIAM Review *59*, 65-98. 10.1137/141000671.
S4. Rackauckas, C., and Nie, Q. (2017). Differentialequations. jl–a performant and feature-rich ecosystem for solving differential equations in julia. Journal of open research software *5*, 15-15.
S5. Rackauckas, C., and Nie, Q. (2017). ADAPTIVE METHODS FOR STOCHASTIC DIFFERENTIAL EQUATIONS VIA NATURAL EMBEDDINGS AND REJECTION SAMPLING WITH MEMORY. Discrete Continuous Dyn Syst Ser B *22*, 2731-2761. 10.3934/dcdsb.2017133.
S6. Skilling, J. (2006). Nested sampling for general Bayesian computation.
S7. Fjelde, T.E., Xu, K., Widmann, D., Tarek, M., Pfiffer, C., Trapp, M., Axen, S.D., Sun, X., Hauru, M., and Yong, P. (2025). Turing. jl: a general-purpose probabilistic programming language. ACM Transactions on Probabilistic Machine Learning.
S8. Feroz, F., Hobson, M., and Bridges, M. (2009). MultiNest: an efficient and robust Bayesian inference tool for cosmology and particle physics. Monthly Notices of the Royal Astronomical Society *398*, 1601-1614.